2-4-2016

Crystal Structure of Deinococcus Phytochrome in the Photoactivated State Reveals a Cascade of Structural Rearrangements during Photoconversion

E Sethe Burgie

Junrui Zhang

Richard D. Vierstra
Washington University in St Louis, rdvierstra@wustl.edu

Article: Structure

Crystal Structure of *Deinococcus* Phytochrome in the Photoactivated State Reveals a Cascade of Structural Rearrangements during Photoconversion

By E. Sethe Burgie[1,2], Junrui Zhang[1], & Richard D. Vierstra[1,2]*

[1]Department of Genetics, University of Wisconsin-Madison, 425-G Henry Mall, Madison, Wisconsin 53706, USA

[2]Department of Biology, Washington University in St Louis, One Brookings Drive, St. Louis, Missouri 63130, USA

*Correspondence should be addressed to: Dr. Richard D. Vierstra

Department of Biology, Campus Box 1137

Washington University in St Louis, One Brookings Drive, St. Louis, Missouri 63130, USA

314-935-5058, office; 314-935-4432, fax

rdvierstra@wustl.edu, email

SUMMARY

Phytochromes are photochromic photoreceptors responsible for a myriad of red/far-red light-dependent processes in plants and microorganisms. Interconversion is initially driven by photoreversible isomerization of bilin, but how this alteration directs the photostate-dependent changes within the protein to actuate signaling is poorly understood. Here, we describe the structure of the *Deinococcus* phytochrome photosensory module in its near complete far-red light-absorbing Pfr state. In addition to confirming the 180° rotation of the D-pyrrole ring, the dimeric structure clearly identifies downstream rearrangements that trigger large-scale conformational differences between the dark-adapted and photoactivated states. Mutational analyses verified the importance of residues surrounding the bilin in Pfr stabilization, and protease-sensitivity assays corroborated photostate alterations that propagate along the dimeric interface. Collectively, these data support a cooperative 'toggle' model for phytochrome photoconversion and advance understandings of the allosteric connection between the photosensory and output modules.

INTRODUCTION

Phytochromes are a diverse collection of photoreceptors in plants and microorganisms that regulate a wide array of light-dependent processes through their unique ability to reversibly interconvert between dark-adapted and photoactivated endstates (Auldridge and Forest, 2011; Burgie and Vierstra, 2014; Franklin and Quail, 2010). They are defined by a covalently-bound bilin (or open chain tetrapyrrole) chromophore cradled within a signature cGMP phosphodiesterase/adenylyl cyclase/FhlA (GAF) domain, which is often bracketed by Period/Arnt/Sim (PAS) and phytochrome-specific (PHY) domains to generate a photosensing module (PSM). The PSM is followed by an output module (OPM); it typically includes a histidine kinase (HK) domain commonly associated with two-component phosphorelays but other OPM arrangements exist (Auldridge and Forest, 2011; Karniol et al., 2005), indicating that the PSM is a uniquely adapted photoswitch capable of initiating a variety of signaling outcomes. The photoactivated state also slowly transitions back to the dark-adapted state by thermal reversion, thus providing a mechanism to dampen the light signal. In most, if not all, cases, phytochromes are arranged as dimers typically in a head-to-head orientation, suggesting that the sister PSMs and OPMs work in concert (Burgie and Vierstra, 2014).

Best known are the phytochromes from higher plants with a canonical PAS-GAF-PHY PSM arrangement (Burgie and Vierstra, 2014; Rockwell et al., 2006). Upon photoexcitation of the bilin, they interconvert between a dark-adapted red-light-absorbing Pr state and a photoactivated far-red light-absorbing Pfr state to ultimately influence nearly all aspects of plant development from seed germination and seedling deetiolation to flowering time and senescence (Franklin and Quail, 2010). Both canonical and variant phytochromes displaying remarkable organizational and photochemical diversities pervade the proteobacterial, cyanobacterial, algal, and fungal clades (Auldridge and Forest, 2011; Burgie and Vierstra, 2014). Included are members of the cyanobacteriochrome photoreceptor (CBCR) subfamily with distinctive GAF domains that can sense other wavelength pairs such as blue/green, blue/orange, and green/red by modification of the bilin, and that sometimes contain tandem arrays of these GAF domains to enable broad color perception (Rockwell et al., 2014; Rockwell et al., 2012; Ulijasz et al., 2009). Also unusual are the proteobacterial bathyphytochromes that use Pfr as the dark-adapted state and require far-red light excitation to generate Pr (Bellini and Papiz, 2012; Giraud et al., 2005; Karniol and Vierstra, 2003; Yang et al., 2008).

How phytochromes allosterically transmit the light signal from the bilin through the PSM and ultimately into the OPM to actuate signaling is not yet clear. The prevailing expectation for most phytochromes is that light absorption by the bilin as Pr induces a *Z*➔*E* isomerization of the

C15=C16 double bond between the C and D pyrrole rings (Burgie et al., 2013; Cornilescu et al., 2014; Kneip et al., 1999; Narikawa et al., 2013; Rudiger et al., 1983; Song et al., 2011; Yang et al., 2009; Yang et al., 2011) concomitant with deprotonation/reprotonation of the pyrrole nitrogens (von Stetten et al., 2007; Wagner et al., 2008). This isomerization rotates the D pyrrole ring, which in turn translates the chromophore within the GAF domain pocket (Cornilescu et al., 2014; Yang et al., 2011). Structural comparisons of the dark-adapted states from canonical phytochromes and bathyphytochrome (Anders et al., 2013; Anders et al., 2014; Burgie et al., 2014a; Burgie et al., 2014b; Yang et al., 2009), along with a recent informative model derived from a mixed Pr/Pfr crystal of the PSM from *Deinococcus radiodurans* bacteriophytochrome (*Dr*-BphP) (Takala et al., 2014) showed that a unique hairpin (or tongue) loop, which extends from the PHY domain to contact the GAF domain, likely rearranges from an anti-parallel β-sheet configuration in Pr to partially α-helical character in Pfr. Reconnection of the Pfr-type hairpin with the GAF domain then induces a tug on opposing helical spines along the dimer interface to splay the sister PHY domains. Presumably, this motion is transmitted into the OPM to reorient the relative positions of the sister motifs that initiate downstream signaling.

While multiple studies support the *Z*➔*E* isomerization of the bilin at the C15=C16 position (at least for canonical Phys), it remains uncertain how this conformational change repositions the bilin, impacts the GAF domain pocket, and ultimately rearranges the adjacent hairpin/GAF domain interface to induce the β-stranded to α-helical hairpin transformation. Moreover, because the splayed *Dr*-BphP PSM structure was generated from a near equal Pr/Pfr mix (Takala et al., 2014), it is unknown if the more 'open' configuration represents the Pfr/Pfr homodimer as well as that of the Pr/Pfr heterodimer, both of which could represent unique signaling states (Furuya and Schafer, 1996). It is also unclear how strongly the OPM restricts PSM movements in light of recent studies that suggest a crosstalk between the two modules (Burgie et al., 2014b; Takala et al., 2015a; Takala et al., 2015b). A particular challenge to resolving these issues by crystallographic approaches is thermal reversion of the photoactivated state, which complicates its maintenance during crystallization trials.

To overcome this hurdle, we exploited here a single amino acid substitution of *Dr*-BphP that greatly attenuates Pfr➔Pr thermal reversion (Burgie et al., 2014b) to generate diffraction quality PSM crystals of a near homogeneous Pfr:Pfr homodimer. The X-ray crystallographic structure of F469W(PSM) as Pfr when compared to prior structures of the wild-type PSM as Pr (Burgie et al., 2014b; Takala et al., 2014) now provides a clear structural view of endstate differences for the bilin and surrounding residues that lead to eventual splaying of the sister PHY domains within the dimer. The relative positions of the PHY domains within the Pfr:Pfr

homodimer superposed well with those in the presumed Pr:Pfr heterodimer previously reported (Takala et al., 2014), implying that the sister subunits work cooperatively in generating the open Pfr conformation even when only one subunit is photoexcited. Together, we clarify the mechanical changes surrounding the bilin after photoconversion and how it might induce large-scale, cooperative movements in the downstream OPMs within the dimeric photoreceptor.

RESULTS

The F469W Mutant is a Suitable Structural Analog for Wild-Type *Dr*-BphP. Our prior mutagenic studies of *Dr*-BphP identified a number of amino acid substitutions that impact the thermal stability of Pfr (Burgie et al., 2014b; Wagner et al., 2008). The most promising for the crystallographic analysis of Pfr was the subtle tryptophan substitution of F469 within the conserved hairpin PRXSF motif given its ability to form and substantially stabilize the Pfr state (Burgie et al., 2014b). The F469W(PSM) polypeptide expressed well in *Escherichia coli,* assembled efficiently with biliverdin *in vitro*, and displayed near normal Pr and Pfr absorption once purified (Figures 1A and 1B). The only difference was a slight decrease in the percentage of Pfr generated under saturating red light as judged by the accentuated shoulder at ~700 nm that represents residual Pr. The Pr and Pfr conformations of the bound biliverdin were also unaffected as judged by near identical circular dichroism (CD) spectra for the mutant versus wild type across wavelengths absorbed by the bilin (Figure 1C). Importantly, Pfr➔Pr thermal reversion was markedly suppressed by ~10 fold relative to that of the wild-type *Dr*-BphP PSM (Figure 1D). Crystallization trials of Pfr-enriched samples (generated by a single pulse of saturating red light) conducted at 4°C to further slow reversion, identified several conditions that eventually generated diffraction quality F469W(PSM) crystals. Based on their absorption spectra, we estimated that 87% of the crystallized chromoproteins were Pfr as compared to the 92% and 89% maxima possible for the wild-type and mutant PSMs in solution, respectively (Figures 1B and 1E).

From a single F469W(PSM) crystal we collected diffraction data of sufficient quality to solve the Pfr structure by molecular replacement, using the prior Pr structures of the wild-type PSM from *Dr*-BphP as search models (Burgie et al., 2014b; Wagner et al., 2005; Wagner et al., 2007). To reduce model bias in the region surrounding biliverdin, it and neighboring side chains were omitted during molecular replacement and initial refinements. X-ray diffraction was mildly anisotropic which limited overall resolution; consequently, we conducted an ellipsoidal truncation of the dataset to 3.4 Å x 3.7 Å x 3.3 Å in the a*, b*, and c* directions, respectively (Figures S1A and S1B; see Tables 1 and S1 for refinement statistics). The asymmetric unit

consisted of two head-to-head dimers; the dimer with the clearest electron density features around the chromophore was described here with the two subunits designated as A and B. The PAS and GAF domains of subunits C and D in the second less-resolved dimer appear to have more conformational freedom, which might have generated the observed anisotropy. Surprisingly, the $P2_12_12_1$ space group and unit cell size for the F469W(PSM) crystals were similar to that reported for a mixed Pr:Pfr crystal of the wild-type PSM despite using different crystallization conditions (Takala et al., 2014). However, whereas the prior study could not resolve the conformation(s) of the bilin and surrounding amino acids, nearly all of the PSM was reasonably well interpreted here, including the bilin, key side chains abutting the bilin, and the hairpin (Figures 2A, 2B, S1C, S1D, S1E and S1F), possibly due to the more homogeneous spectral character of the crystallized chromoproteins (87% Pfr/Ptotal here versus 52% estimated for the mixed crystal (Figure 1E; Takala et al., 2014)).

Chromophore Conformation and Configuration of the Bilin-Binding Pocket as Pfr. The Pfr bilin from canonical phytochromes was predicted to have a $5Z_{syn}10Z_{syn}15E_{anti}$ (*ZZEssa*) configuration generated from the *ZZZssa* Pr configuration by photoisomerization of the C15=C16 double bond and rotation of the D pyrrole ring (Kneip et al., 1999; Rudiger et al., 1983; Song et al., 2011). We definitively confirmed this conformational switch for *Dr*-BphP based on both the electron density of biliverdin and the positions of neighboring amino acid side chains for the Pfr model described here as compared with prior Pr models (Figures 2C and 2D; Burgie et al., 2014b; Wagner et al., 2005; Wagner et al., 2007)). The overall configuration of the bilin, including the upward tilt of the D pyrrole ring relative to the more planar A-C rings and the positioning of the propionate side chains, was remarkably congruent with prior structures generated for the Pfr ground states from the bathyphytochromes *Pseudomonas aeruginosa* BphP (Yang et al., 2009) and *Rhodopseudomonas palustris* BphP1 (Bellini and Papiz, 2012), thus reinforcing the notion that canonical and bathyphytochromes employ similar photointerconversion mechanisms (Figure S2A).

Detailed comparisons of the bilin electron densities within the unit cell detected greater structural heterogeneity for the B Subunit. Whereas the biliverdin moiety in Subunit A could be modeled with a single *ZZEssa* Pfr conformation, modeling it into Subunit B generated substantial Fo-Fc difference density features (Figure S3). The major Pfr conformer in Subunit B, exhibits a different C-ring propionate position than that seen for Subunit A. Here, it acquires a more 'Pr-like' position, which includes contacts of the carboxylate with S272 and S274 (Figure S3). Moreover, the difference electron density for the Subunit B chromophore suggests a

second conformation that matches C-ring propionate position in Subunit A (Figure S3). Together, these observations revealed structural asymmetry in the conformation of the bilin and surrounding amino acids across Pfr-enriched homodimers and might even imply the detection of residual Pr species in the crystal.

Close inspection of the bilin-binding pocket for the paired Pr and Pfr endstates now allows a detailed proposal for the initial steps in Pr➔Pfr photoconversion. The D ring flip produces a high energy binding state for the bilin, originating from the amphipathic nature of the D pyrrole ring and its immediate environment within the binding pocket. This unfavorable situation is rectified as the suite of hydrogen bonds tethering biliverdin within the GAF domain pocket ruptures to permit a new set of contacts, many of which are encouraged as the bilin slides through a rotary motion with the thioether linkage between cysteine-24 and the $C3^2$ carbon acting as a hinge (Figures 2C and 2D). For Subunit A, the two biliverdin propionates retain much of their overall conformations, but completely exchange interaction partners within the GAF domain. The B pyrrole ring propionate hydrogen bonds with R254 and Y216 as Pr but switches to R222 as Pfr, whereas the C pyrrole ring propionate hydrogen bonds with S272 and S274 as Pr but switches in part to S272, H290, and Y176 as Pfr (Figures 2A and 2C).

To achieve this new configuration, the R222 side chain undergoes a large rotameric change, and the Y176 sidechain swivels 120°, a motion that is coincident with rotation of the F203 and H201 sidechains (Figure 2C). Rotation of H201 appears especially critical as it enables a switch of the hydrogen bond between the D pyrrole ring carbonyl and H290 in Pr to one with H201, which then anchors its Pfr position. The importance of both Y176 and H201 in maintaining the Pfr conformation is vividly illustrated by several site-directed PSM mutants, which compromise full Pr➔Pfr photoconversion and either dramatically suppress or accelerate Pfr➔Pr thermal reversion, respectively (Figures 2E and 2F). H290 is also central to the stability of both photostates; it binds the D-ring carbonyl as Pr and subsequently anchors the Pfr bilin position by interacting with the C-ring propionate (Figures 2A and 2C). As described above, the C-ring propionate in Subunit B appears to assume two alternate conformations as Pfr, one that mimics that of Subunit A and a second in which it extends backward to interact with S272 and S274 (Figures 2B and S3). As with the bilin, substantial Fo-Fc difference density was detected in Subunit B surrounding side chains of R222, Y176, F203, and H201, consistent with Pfr heterogeneity and the possible presence of Pr in the crystal lattice.

Contacts between the GAF domain and PHY domain hairpin were also altered upon photoconversion. In Pr, the carboxylate of D207 is doubly hydrogen bonded with R466 in the hairpin PR*X*SF motif, whereas this contact is replaced in Pfr by hydrogen bonds between D207

and S468 in the same hairpin motif, and Y263 in the GAF domain, which moves closer to the hairpin as the D ring flips and slides (Figure 2C). Through all these reconfigurations, the hydrogen bonding lattice involving the A-C ring pyrrole nitrogens, the imidazole of H260, the main chain carbonyl of D207, and the pyrrole water appears to be maintained (Figure 2C).

Large Scale Conformational Changes in the PSM. With the exception of a few residues (1-6, 454-459 of Subunit A; 1-6, 346-347, 452-459 of Subunit B), the F469W(PSM) model provides a complete snapshot of the *Dr*-BphP PSM as Pfr, including a head-to-head dimer arrangement, a figure-of-eight knot connecting the PAS and GAF domains, and a well resolved α-helical hairpin extending from the PHY domain (Figure 3A). This structure is strikingly similar to the mixed Pr:Pfr structure we estimated to contain ~52% Pfr (Takala et al., 2014); in fact, the two dimeric models superpose reasonably well with a RMSD of 1.1 Å over 905 Cα atoms (Figure S2C). Unlike the anti-parallel β-sheet conformation of the hairpin stem that abuts the GAF domain surface as Pr (Burgie et al., 2014b; Takala et al., 2014), the two stem segments of the Pfr hairpin rotate to generate a new complement of hairpin/GAF domain interactions, with the exit strand of the hairpin assuming a helical conformation and the entrance strand adopting random coil (Figures 3A, S1E and S1F). The hairpin contacts the GAF domain through A450 and W451 in the hairpin entrance strand and the predominantly hydrophobic side of the hairpin helix (includes P465, F469W and Y472) associating at or near strand β3 and helix α4, and through hydrogen bonds between S468 in the hairpin helix and D207 and Y263 in the GAF domain. It also appears that P465 contacts the vinyl side group in the D pyrrole ring of biliverdin (Figure S1F).

As seen previously with the mixed Pr/Pfr crystal (Takala et al., 2014), the sister PHY domains are substantially splayed relative to those in Pr, which appears to be generated by the β-strand to α-helical transition of the hairpin stem, novel hairpin/GAF domain contact points, and straightening of the helical spine bow centered at A326 (Figures 3A and 3B). The two subunits still retain some of the left-handed helical twist seen for Pr but now with significant outward displacement such that the distance between sister Cα atoms of H334 and T499 is extended by 10.5 Å and 22 Å, respectively. The α-helical character for the *Dr*-BphP hairpin stem and its contacts to the GAF domain are remarkably similar to those from *P. aeruginosa* BphP and *R. palustris* BphP1 (Figure S2B (Bellini and Papiz, 2012; Yang et al., 2009)), thus reinforcing the conserved feature of this Pfr conformation. However, when the complete PSM dimer of *Dr*-BphP as Pfr was overlaid with that from *P. aeruginosa* BphP as Pfr (Yang et al., 2009), the relative orientation of the sister PSMs differed substantially, suggesting either inherent

variations in the dimerization interface or artifactual alterations induced by crystal packing of these likely flexible regions (Figure S2D).

The Helical Spine is Perturbed by Photoconversion. Current models for phytochrome photoconversion posit that bilin-driven reorganization of the hairpin induces an outward splay of the sister PHY domains, which is transmitted into the OPMs along the helical spine that presumably spans the length of each subunit (Figures 4B and 4E; Anders et al., 2013; Burgie and Vierstra, 2014; Burgie et al., 2014b; Takala et al., 2014; Yang et al., 2009). To probe the extent of these photo-state induced perturbations, we replaced informative sections of the spine with tobacco etch virus (TEV) protease recognition sites (Figure 4A), and assayed for their susceptibility to TEV protease cleavage in either the Pr state or following saturating red-light irradiation (mostly Pfr). Included were positions examining the GAF/GAF helical dimerization contact (TEV-150), and accessibility of the helical spine either connecting the GAF and PHY domains (TEV-328), within the PHY domain (TEV-341), at the junction between the PHY and HK domains (TEV-501), or at a previously studied site proximal to the phosphoacceptor histidine (H532) in the HK region (TEV-518) (Li et al., 2010) (Figures 4A and 4C). Whereas the sites within the PSM could be accurately positioned into current PSM models (Burgie et al., 2014b; Takala et al., 2014; Wagner et al., 2007), the TEV-501 and TEV-518 sites were predicted from a PSM/OPM chimera generated by connecting the helical spine from the *Dr*-BphP PSM as Pr to the DHp helical bundle in the dimeric HK domain from *Thermotoga maritima* HK853 (Casino et al., 2009). As shown in Figures 4B and 4C, the left-hand twisted pseudomolecule was remarkably similar in shape to that determined from single particle EM images of full-length *Dr*-BphP (Burgie et al., 2014b; Li et al., 2010).

All five TEV-site mutants expressed well recombinantly, assembled with biliverdin, and generated absorption spectra nearly indistinguishable from unmodified full-length *Dr*-BphP as Pr or Pfr (Figure S4A). Only the rates of thermal reversion showed substantial variations (Figure S4B), which were negated by conducting the TEV protease assays for Pfr under continuous red-light irradiation. We note that the kinetics for most of the cleavage reactions were described by the sum of two exponentials that could reflect conformational heterogeneity, and/or differential protease susceptibility of either the Pr:Pfr heterodimers versus Pfr:Pfr homodimers or between the initial uncleaved dimer and its singly cleaved product.

Collectively, the TEV protease assays confirmed substantial reorganization of the sister PSMs during photoconversion, much of which agreed with single particle EM images of Pr and Pfr (Figure 4B; Burgie et al., 2014b). The TEV-150 site was highly resistant to cleavage in

either spectral state when introduced into either the PSM alone or into the full-length chromoprotein (Figure 4D), consistent with this site being buried within the six-helix bundle dimerization contact between GAF domains, and the predicted rigid nature of this connection (Burgie et al., 2014b; Takala et al., 2014; Wagner et al., 2007). As expected, the TEV-328 site was strongly susceptible to cleavage given the separation of the sister PHY domains in this region (Burgie et al., 2014b; Li et al., 2010; Takala et al., 2014). However, whereas the PSM construction as Pfr was slightly less sensitive to TEV protease cleavage than Pr (0.31 fold), more comparable rates between Pr and Pfr were seen in the full-length chomoprotein, implying that the OPM influences the conformation of this section of the helical spine.

The TEV-341 and TEV-518 sites within the PHY domain and adjacent to the phosphoacceptor histidine, respectively, showed robust changes in TEV protease sensitivity with the Pfr form being digested 9.5 and 40 times faster, respectively, consistent with strong increases in solvent accessibility around these regions upon photoconversion. However, the TEV-501 site, although still susceptible to cleavage, showed little difference between Pr and Pfr, suggesting that while the helical spine below and above this region are substantially impacted by photoconversion, this TEV-501 segment is not (Figure 4D). Collectively, it appears that the OPM modifies the amplitude of the splay that is presented by the Pr and Pfr crystal structures and X-ray scattering analyses of the PSM (Figures 3A and 3B; Takala et al., 2014), and suggests that some positions along the helical spine might remain tethered as shown by the single particle EM images of full-length Pfr dimers (Figure 4B; Li et al., 2010). For example, the helical spine near residue 501 could remain in contact with that of its sister subunit, whereas positions not too far proximal or distal separate (*e.g.,* position 341 and 518) (Figure 4E).

DISCUSSION

Recent advances in the structure and photochemistry of phytochromes have greatly improved our understanding of these photosensors and point to a 'toggle' model for photoconversion in which *Z*➔*E* isomerization of the C15=C16 double bond in the bilin triggers its sliding within the binding pocket and concomitant reorientation of adjacent residues (Anders et al., 2013; Burgie and Vierstra, 2014; Yang et al., 2009). The combined motions are followed by structural remodeling of the hairpin and its contact with the GAF domain to eventually splay the helical spine of sister PHY domains, the motion of which is ultimately translated further up the helical spine to allosterically induce OPM activation/deactivation (Burgie et al., 2014b; Takala et al., 2014). Our paired Pr and Pfr structures of the *Dr*-BphP PSM enhanced the resolution of this model by now permitting visualization of most, if not all, critical features. Here, we exploited the

F469W mutation to enable crystallization of near homogeneous Pfr:Pfr dimers, which appeared to have little impact on the bilin and GAF-domain/hairpin interactions despite substantially stabilizing the Pfr state. An unanticipated outcome was the detection of chromophore asymmetry within the Pfr dimer, which is consistent with prior spectroscopic studies on bacterial phytochromes that noticed multiple conformations for the Pfr bilin (Salewski et al., 2013). At least with respect to *Dr*-BphP, there appears to be sufficient local mobility within the GAF domain pocket to accommodate at least two Pfr conformations of biliverdin that differ with respect to the C-pyrrole ring propionate. The extent to which such subtle plasticity might impact bilin photochemistry is unknown.

In addition to confirming the *ZZZssa* to *ZZEssa* isomerization of the bilin, the paired structures also clarified the importance of the hydrogen bond network tethering biliverdin within the GAF domain. This network tracks with bilin movement to eventually instigate remodeling of the adjacent hairpin. This is especially evident for Y263, which is pushed toward the hairpin through these movements and by the D-ring itself. H290 and H201 are also key to photoconversion and the stability of both photostates by anchoring the Pr and Pfr bilin configurations, respectively. Substitutions of H290 generate highly fluorescent, photochemically crippled Pr (Wagner et al., 2008), whereas substitutions of H201 attenuate Pr➔Pfr photoconversion and destabilizes the Pfr endstate (this report). The comparable 201 position among phytochromes with Pr dark-adapted states is typically reserved for hydrophobic residues, whereas bathyphytochromes often have hydrophilic residues such as glutamine (*P. aeruginosa* BphP) or asparagine (*R. palustris* BphP1) that potentially act as hydrogen bond donors for the D-ring carbonyl. The importance of residue 201 might explain why *Dr*-BphP with H201 has an unusually stable Pfr state, and why the Q188L substitution at the same site in the *P. aeruginosa* bathyphytochrome BphP yields a more stable Pr state after Pfr➔Pr photoconversion (Yang et al., 2009). With the exception of a slight displacement of D207, the hydrogen bond lattice anchoring the pyrrole water is unaffected by photoconversion, suggesting that its main function is to position this water as a suitable proton acceptor/donor during the early deprotonation/protonation cycle of the bilin (Velazquez Escobar et al., 2015; von Stetten et al., 2007; Wagner et al., 2008).

The hydrophobic residues surrounding the D pyrrole ring (Y176, F203, and Y263) were long regarded as important to photoconversion likely by providing an adjustable hydrophobic environment to support the amphiphatic D pyrrole ring as both Pr and Pfr (Wagner et al., 2005). Our paired structures now help explain their influence by showing that all three swivel during photoconversion, with Y176 and F203 displaying substantial side chain rotation that

concomitantly permits H201 to rotate and engage the D-ring carbonyl as Pfr. The importance of Y176 was previously shown by histidine substitutions that generate Pr-locked, highly fluorescent variants in several Phys (Fischer and Lagarias, 2004; Wagner et al., 2005). Roles for R254, R222, S274 and S272 during photoconversion were also clarified here as they collectively maintain contact with the propionate side chains of the B and C pyrrole rings as the bilin slides during photoconversion.

Based on an assemblage of Pr and Pfr structures (Anders et al., 2013; Burgie et al., 2014b) along with the mixed Pr:Pfr structure of *Dr*-BphP(PSM) (Takala et al., 2014), it was expected that the GAF domain/hairpin connection reorganizes during photoconversion as a result of a β-stranded to α-helical hairpin stem transformation. Our Pfr structure confirms the impetus for this change that includes the transitions described above around the D-pyrrole ring to promote the swap of GAF/hairpin hydrogen bond partners from D207/R466 to D207+Y263/S468.

Comparisons of the GAF domain pocket of *Dr*-BphP in its photoactivated Pfr state to that from the two bathyphytochromes in their dark-adapted Pfr state revealed remarkable similarities in chromophore conformation (particularly for Subunit A), positioning and amino acid contacts, and α-helical hairpin architecture (this report (Anders et al., 2013; Bellini and Papiz, 2012; Yang et al., 2008, 2009; Yang et al., 2011)), strongly implying that these distinct phytochrome subfamilies employ analogous photointerconversion mechanisms despite starting from opposite dark-adapted states. In fact, mutant analyses suggest that only a few amino acid replacements are required to switch the preferred spectral state of a dark-adapted chromoprotein. Possible residues include A288 and R254 where substitutions in *A. thaliana* PhyB (Burgie et al., 2014a) and *Dr*-BphP (Wagner et al., 2008) generate highly stable Pfr states, and the Q188L substitution in *P. aeruginosa* bathyphytochrome BphP which slows thermal reversion of Pr back to Pfr (Yang et al., 2009). Further structural comparisons of *Dr*-BphP to the *Thermosynechococcus elongatus* blue/green-light photointerconvertible CBCR PixJ also suggest that at least some CBCRs employ a similar photoconversion mechanism, which includes D-ring rotation and bilin sliding, despite lacking both the PAS and PHY domains (Burgie et al., 2013; Cornilescu et al., 2014; Narikawa et al., 2013).

A surprising observation was that our *Dr*-BphP PSM structure at near full Pfr occupancy superposed well with that for a possibly equimolar Pr:Pfr mix (Takala et al., 2014). Both structures resolved matching helical hairpins within the dimer despite the likelihood that one subunit in the Pr:Pfr mix still retained the Pr bilin conformation. The most parsimonious explanation is that the *Dr*-BphP subunits work cooperatively; *i.e.,* when one transitions to the Pfr

bilin and protein conformations, the sister subunit follows spontaneously without photoactivation to assume a 'Pfr'-type protein fold even though it contains a Pr bilin. As such, each phytochrome subunit could be delicately balanced between Pr and Pfr thus allowing the paired subunits to strongly influence each other's folds as they switch between endstates either by photoactivation or thermal reversion. Hints of this cooperativity can be found in Pfr➔Pr thermal reversion assays, which often require at least two exponentials to describe their rates (Burgie et al., 2014b; Hennig and Schafer, 2001; Takala et al., 2015a; Takala et al., 2015b), and in previous spectral studies on several canonical bacterial phytochromes that only reach 50% photoconversion under saturating red-light (Burgie et al., 2014b; Shah et al., 2012). With respect to signaling, such cooperativity might explain why some phytochrome responses can be driven by very low light fluences theoretically capable of photoactivating only one subunit in the dimer (Possart et al., 2014). A disconnection between the 'Pfr' protein fold and the spectral state of the bilin might also explain the phenotypic effect of the Y276H mutant of *A. thaliana* PhyB that is able to activate photomophorgenesis in the absence of light (Rausenberger et al., 2011; Su and Lagarias, 2007). Despite the bilin being locked in Pr, the mutant presumably assumes a Pfr-like state with respect to signaling.

Finally, we confirm predictions that the helical spine extending into the OPM is influenced by photoconversion but found that positions along the spine might be impacted differentially. The PAS/GAF dimer interface, which appears unaffected by photoconversion, likely provides a strong foundation to direct the conformational signal toward the PSM, which is also made more rigid by the PAS/GAF knot link. The helix connecting the GAF and PHY domains is perturbed as predicted by the splaying of PHY domains in the crystal structures (this work; Takala et al., 2014). The exposed TEV-328 site exhibits only small changes in protease sensitivity upon photoconversion of the full-length photoreceptor, but these changes are enhanced in the PSM construction, showing that the OPM has a non-trivial effect on PSM conformation/function. The putative helical region just downstream of the PHY domain, which is exemplified by TEV-501, shows little to no light-dependent changes in protease sensitivity, while the region approaching the HK OPM proper (TEV-518) shows massive change. Together with the single particle EM models of full-length *Dr*-BphP and analyses of PSM dimerization with and without the OPM (Burgie et al., 2014b; Li et al., 2010; Takala et al., 2015b), the data argue for some retention of the sister OPM contacts along the helical spine as opposed to complete dissociation. One possibility is that the OPM reorients in a scissors-like motion centered around residue 501 to generate large-scale disturbances of the sister HK domains, which is detected as a complete splay if only the PSM is analyzed (Figure 4E). Clearly, the now available Pr and Pfr

structures of the *Dr*-BphP PSM should help identify residues whose modification could enhance or discourage various aspects of phytochrome dynamics (*e.g.,* photoconversion, thermal reversion, and fluorescence) and OPM activation for gains in agriculture, cell biology and optogenetics.

EXPERIMENTAL PROCEDURES

Dr-BphP Protein Expression and Purification

Full-length *D. radiodurans* BphP (*Dr*-BphP) chromoproteins (755 residues), and PSM (residues 1-501) constructions bearing a TEV recognition site bore an N-terminal T7 tag (MASMTGGQQMGRGS) and a C-terminal FLAG/hexahistidine tag (GGGDYKDDDDKLEHHHHHH) (Burgie et al., 2014b; Wagner et al., 2008). All other constructions included an N-terminal T7 tag, the PSM, and a C-terminal hexahistidine tag (LEHHHHHH). For TEV-protease sensitivity assays (Li et al., 2010), the TEV-protease recognition site (ENLYFQG) replaced the wild-type amino acid sequence such that the scissile Q-G sequence was at position 150-151, 328-329, 341-342, 501-502, or 518-519. Protein expression and purification were conducted as described previously (Burgie et al., 2014b) with slight modifications as described in the Supplemental Experimental Procedures.

Buffer exchanges were conducted with 30 kDa MWCO centrifugal filters (Merck Millipore). *Dr*-BphP samples destined for assays were exchanged into 50 mM HEPES-KOH (pH 7.8 at 25 °C) and 150 mM KCl, while *Dr*-BphP(F469W) chromoproteins used for crystallography were exchanged into 150 mM NaCl, and 20 mM MOPS-NaOH (pH 7.0). Samples were frozen as 30-µl droplets in liquid nitrogen, and stored at −80 °C. Covalent binding of BV to the *Dr*-BphP apoproteins was monitored by zinc-induced fluorescence of the chromoproteins following SDS-PAGE (Davis et al., 1999).

Crystallization of the *Dr*-BphP(F469W) PSM in the Pfr conformer

Crystals of the F469W mutant as Pfr were grown by sitting drop vapor diffusion at 4°C after mixing 200 nl of F469W at 30 mg/ml with 200 nl of reservoir solution (12% polyethylene glycol 3350, 200 mM ammonium acetate, 5% fructose, 5% glucose, and 100 mM sodium citrate (pH 5.6)), and irradiating samples with a single red LED pulse (635 nm maximum, Super Bright LEDs) for 30 min. Thereafter, samples were incubated in darkness, and all sample or crystal manipulations were conducted under a green LED light source (525 nm maximum, Super Bright LEDs, Inc.). Before flash-cooling in liquid nitrogen, the crystals were soaked with 13%

polyethylene glycol 3350, 200 mM ammonium acetate, 5% fructose, 5% glucose, 18% ethylene glycol, and 100 mM sodium citrate (pH 5.6).

X-ray Crystallography and Structure Refinement

X-ray diffraction data for the Pfr state of F469W(PSM) were collected at the Advanced Photon Source, Life Sciences Collaborative Access Team 21-ID-F beamline at Argonne National Laboratory. Datasets were indexed, integrated, and scaled with XDS (Kabsch, 2010). The data were then truncated via the UCLA-DOE Laboratory Diffraction Anisotropy Server using default parameters (F/sigma>3) and B-factor sharpening (Strong et al., 2006). Molecular replacement was conducted with PHASER (McCoy et al., 2007) using as search models residues 6-328 and residues 328-506 from the PAS-GAF and PSM models, respectively, of *Dr*-BphP as Pr (PDB ID codes 2O9C (Wagner et al., 2007) and 4Q0J (Burgie et al., 2014b)). The search model excluded residues 446-477 of the hairpin and biliverdin, while 24 residues flanking biliverdin were modeled as alanines. Data refinement included standard methodologies as described in Supplemental Experimental Procedures.

Spectroscopic and Thermal Reversion Measurements

Spectral and thermal reversion data were collected as described previously (Burgie et al., 2014b). See Supplemental Experimental Procedures for details. CD spectra of samples at 25°C were recorded in 1 nm steps with an averaging time of 0.5 sec using a AVIV Model 420 circular dichroism spectrometer (Aviv Biomedical).

Tobacco Etch Virus Protease Sensitivity Assays

Dr-BphP-TEV constructions were assayed for TEV protease cleavage at 25°C in 150 mM KCl, 1 mM TCEP, and 50 mM HEPES-KOH (pH 7.8 at 25°C) (Li et al., 2010). Each assay contained the chromoprotein at a final absorbance of 0.9 for the Q band, and 0.4 mg/ml TEV protease expressed recombinantly (Burgie et al., 2014a). Reactions were conducted in darkness (Pr) or under constant red-light irradiation (635 nm peak output, Super Bright LEDs), and was quenched by mixing equal volumes of sample with SDS-PAGE sample buffer (4% sodium dodecyl sulfate, 20% (v/v) glycerol 0.2 mg/ml bromophenol blue, 10% 2-mercaptoethanol, and 125 mM Tris-HCl (pH 6.7)), followed by heating to 100°C for 3 min. Following SDS-PAGE, the relative levels of the substrate *Dr*-BphP and products were imaged using an Epson Perfection 3170 Photo scanner (Epson America) and quantified with Quantity One, version 4.6.9 (Bio-Rad).

ACCESSION NUMBERS

Atomic coordinates for the PSM of *Dr*-BphP(F469W) as Pfr have been deposited in the Protein Data Bank (PDB ID code 5C5K). Correspondences and requests for materials should be addressed to R.D.V. (rdvierstra@wustl.edu) or E.S.B. (esburgie@wustl.edu)

SUPPLEMENTAL INFORMATION

Supplemental Information includes Supplemental Experimental Procedure and four figures and can be found with this article at http://xxxxxxxxxx.

AUTHOR CONTRIBUTIONS

E.S.B. and R.D.V. conceived the project, designed the experiments, and wrote the paper. E.S.B. solved the structure and generated all other data. J.Z. provided methodologies and gene constructions associated with the TEV protease cleavage assays.

ACKNOWLEDGMENTS

We acknowledge beamline access from the Advanced Photon Source, Life Sciences Collaborative Access Team 21-ID-F, and GM/CA Collaborative Access Team 23-ID-B at Argonne National Laboratory, and the National Synchrotron Light Source beamlines X25 and X26C at Brookhaven National Laboratories. We thank Drs. Allen Orville and Babak Andi for initial screening of crystal diffraction, Dr. Craig Bingman for use of the Mosquito crystallization robot, and Joseph Walker for technical assistance. We acknowledge the Biophysics Instrumentation Facility at the University of Wisconsin-Madison for access to CD instrumentation, and Dr. Darrell McCauslin for technical help. This work was supported by the US National Science Foundation grant MCB-1329956 to R.D.V.

REFERENCES

Anders, K., Daminelli-Widany, G., Mroginski, M., von Stetten, D., and Essen, L. (2013). Structure of the cyanobacterial phytochrome 2 photosensor implies a tryptophan switch for phytochrome signaling. J Biol. Chem. *288*, 35714-35725.

Anders, K., Gutt, A., Gaertner, W., and Essen, L.O. (2014). Phototransformation of the red-light sensor cyanobacterial phytochrome 2 from *Synechocystis* sp. depends on its tongue motifs. J. Biol. Chem. *289*, 25590-25600.

Auldridge, M.E., and Forest, K.T. (2011). Bacterial phytochromes: more than meets the light. Crit. Rev. Biochem. Mol. Biol. *46*, 67-88.

Bellini, D., and Papiz, M.Z. (2012). Structure of a bacteriophytochrome and light-stimulated protomer swapping with a gene repressor. Structure *20*, 1436-1446.

Burgie, E.S., Bussell, A.N., Walker, J.M., Dubiel, K., and Vierstra, R.D. (2014a). Crystal structure of the photosensing module from a red/far-red light-absorbing plant phytochrome. Proc. Natl. Acad. Sci. USA *111*, 10179-10184.

Burgie, E.S., and Vierstra, R.D. (2014). Phytochromes: an atomic perspective on photoactivation and signaling. Plant Cell *26*, 4568-4583.

Burgie, E.S., Walker, J.M., Phillips, G.N.J., and Vierstra, R.D. (2013). A photo-labile thioether linkage to phycoviolobilin provides the foundation for the blue/green photocycles in DXCF-cyanobacteriochromes. Structure *21*, 88-97.

Burgie, E.S., Wang, T., Bussell, A.N., Walker, J.M., Li, H., and Vierstra, R.D. (2014b). Crystallographic and electron microscopic analyses of a bacterial phytochrome reveal local and global rearrangements during photoconversion. J. Biol. Chem. *289*, 24573-24587.

Casino, P., Rubio, V., and Marina, A. (2009). Structural insight into partner specificity and phosphoryl transfer in two-component signal transduction. Cell *139*, 325-336.

Cornilescu, C.C., Cornilescu, G., Burgie, E.S., Markley, J.L., Ulijasz, A.T., and Vierstra, R.D. (2014). Dynamic structural changes underpin photoconversion of a blue/green cyanobacteriochrome between its dark and photoactivated states. J. Biol. Chem. *289*, 3055-3065.

Davis, S.J., Vener, A.V., and Vierstra, R.D. (1999). Bacteriophytochromes: phytochrome-like photoreceptors from nonphotosynthetic eubacteria. Science *286*, 2517-2520.

Evans, P.R., and Murshudov, G.N. (2013). How good are my data and what is the resolution? Acta Cryst. *D69*, 1204-1214.

Fischer, A.J., and Lagarias, J.C. (2004). Harnessing phytochrome's glowing potential. Proc. Natl. Acad. Sci. USA *101*, 17334-17339.

Franklin, K.A., and Quail, P.H. (2010). Phytochrome functions in *Arabidopsis* development. J. Exp. Bot. *61*, 11-24.

Furuya, M., and Schafer, E. (1996). Photoperception and signalling of induction reactions by different phytochromes. Trends Plant Sci. *1*, 301-307.

Giraud, E., Zappa, S., Vuillet, L., Adriano, J.M., Hannibal, L., Fardoux, J., Berthomieu, C., Bouyer, P., Pignol, D., and Vermeglio, A. (2005). A new type of bacteriophytochrome acts in tandem with a classical bacteriophytochrome to control the antennae synthesis in *Rhodopseudomonas palustris*. J. Biol. Chem. *280*, 32389-32397.

Hennig, L., and Schafer, E. (2001). Both subunits of the dimeric plant photoreceptor phytochrome require chromophore for stability of the far-red light-absorbing form. J. Biol. Chem. *276*, 7913-7918.

Kabsch, W. (2010). XDS. Acta Cryst. *D66*, 125-132.

Karniol, B., and Vierstra, R.D. (2003). The pair of bacteriophytochromes from *Agrobacterium tumefaciens* are histidine kinases with opposing photobiological properties. Proc. Natl. Acad. Sci. USA *100*, 2807-2812.

Karniol, B., Wagner, J.R., Walker, J.M., and Vierstra, R.D. (2005). Phylogenetic analysis of the phytochrome superfamily reveals distinct microbial subfamilies of photoreceptors. Biochem J. *392*, 103-116.

Kneip, C., Hildebrandt, P., Schlamann, W., Braslavsky, S.E., Mark, F., and Schaffner, K. (1999). Protonation state and structural changes of the tetrapyrrole chromophore during the Pr --> Pfr phototransformation of phytochrome: a resonance Raman spectroscopic study. Biochemistry *38*, 15185-15192.

Li, H., Zhang, J., and Vierstra, R.D. (2010). Quaternary organization of a phytochrome dimer as revealed by cryoelectron microscopy. Proc. Natl. Acad. Sci. USA *107*, 10872-10977.

McCoy, A., Grosse-Kunstleve, R., Adams, P., Winn, M., Storoni, L., and Read, R. (2007). Phaser crystallographic software. J. Appl. Crystallogr. *40*, 658-674.

Narikawa, R., Ishizuka, T., Muraki, N., Shiba, T., Kurisu, G., and Ikeuchi, M. (2013). Structures of cyanobacteriochromes from phototaxis regulators AnPixJ and TePixJ reveal general and specific photoconversion mechanism. Proc. Natl. Acad. Sci. USA *110*, 918-923.

Possart, A., Fleck, C., and Hiltbrunner, A. (2014). Shedding (far-red) light on phytochrome mechanisms and responses in land plants. Plant Sci. *217-218*, 36-46.

Rausenberger, J., Tscheuschler, A., Nordmeier, W., Wust, F., Timmer, J., Schafer, E., Fleck, C., and Hiltbrunner, A. (2011). Photoconversion and nuclear trafficking cycles determine phytochrome A's response profile to far-red light. Cell *146*, 813-825.

Rockwell, N.C., Duanmu, D., Martin, S.S., Bachy, C., Price, D.C., Bhattacharya, D., Worden, A.Z., and Lagarias, J.C. (2014). Eukaryotic algal phytochromes span the visible spectrum. Proc. Natl. Acad. Sci. USA *111*, 3871-3876.

Rockwell, N.C., Martin, S.S., and Lagarias, J.C. (2012). Mechanistic insight into the photosensory versatility of DXCF cyanobacteriochromes. Biochemistry *51*, 3576-3585.

Rockwell, N.C., Su, Y.S., and Lagarias, J.C. (2006). Phytochrome structure and signaling mechanisms. Annu. Rev. Plant. Biol. *57*, 837-858.

Rudiger, W., Thummler, F., Cmiel, E., and Schneider, S. (1983). Chromophore structure of the physiologically active form (P(fr)) of phytochrome. Proc. Natl. Acad. Sci. USA *80*, 6244-6248.

Salewski, J., Escobar, F.V., Kaminski, S., von Stetten, D., Keidel, A., Rippers, Y., Michael, N., Scheerer, P., Piwowarski, P., Bartl, F.*, et al.* (2013). Structure of the biliverdin cofactor in the Pfr state of bathy and prototypical phytochromes. J. Biol. Chem. *288*, 16800-16814.

Shah, R., Schwach, J., Frankenberg-Dinkel, N., and Gartner, W. (2012). Complex formation between heme oxygenase and phytochrome during biosynthesis in *Pseudomonas syringae* pv. tomato. Photochem. Photobiol. Sci. *11*, 1026-1031.

Song, C., Psakis, G., Lang, C., Mailliet, J., Gartner, W., Hughes, J., and Matysik, J. (2011). Two ground state isoforms and a chromophore D-ring photoflip triggering extensive intramolecular changes in a canonical phytochrome. Proc. Natl. Acad. Sci. USA *108*, 3842-3847.

Strong, M., Sawaya, M.R., Wang, S., Phillips, M., Cascio, D., and Eisenberg, D. (2006). Toward the structural genomics of complexes: crystal structure of a PE/PPE protein complex from *Mycobacterium tuberculosis*. Proc. Natl. Acad. Sci. USA *103*, 8060-8065.

Su, Y.S., and Lagarias, J.C. (2007). Light-independent phytochrome signaling mediated by dominant GAF domain tyrosine mutants of *Arabidopsis* phytochromes in transgenic plants. Plant Cell *19*, 2124-2139.

Takala, H., Bjorling, A., Berntsson, O., Lehtivuori, H., Niebling, S., Hoernke, M., Kosheleva, I., Henning, R., Menzel, A., Ihalainen, J.A.*, et al.* (2014). Signal amplification and transduction in phytochrome photosensors. Nature *509*, 245-248.

Takala, H., Bjorling, A., Linna, M., Westenhoff, S., and Ihalainen, J.A. (2015a). Light-induced changes in the dimerization interface of bacteriophytochromes. J. Biol. Chem. *290*, 16383-16392

Takala, H., Lehtivuori, H., Hammaren, H., Hytonen, V.P., and Ihalainen, J.A. (2015b). Connection between absorption properties and conformational changes in *Deinococcus radiodurans* phytochrome. Biochemistry *53*, 7076-7085.

Ulijasz, A.T., Cornilescu, G., von Stetten, D., Cornilescu, C., Velazquez Escobar, F., Zhang, J., Stankey, R.J., Rivera, M., Hildebrandt, P., and Vierstra, R.D. (2009). Cyanochromes are blue/green light photoreversible photoreceptors defined by a stable double cysteine linkage to a phycoviolobilin-type chromophore. J. Biol. Chem. *284*, 29757-29772.

Velazquez Escobar, F., Piwowarski, P., Salewski, J., Michael, N., Fernandez Lopez, M., Rupp, A., Muhammad Qureshi, B., Scheerer, P., Bartl, F., Frankenberg-Dinkel, N.*, et al.* (2015). A protonation-coupled feedback mechanism controls the signalling process in bathyphytochromes. Nature Chem. *7*, 423-430.

von Stetten, D., Seibeck, S., Michael, N., Scheerer, P., Mroginski, M.A., Murgida, D.H., Krauss, N., Heyn, M.P., Hildebrandt, P., Borucki, B.*, et al.* (2007). Highly conserved residues D197 and H250 in Agp1 phytochrome control the proton affinity of the chromophore and Pfr formation. J. Biol. Chem. *282*, 2116-2123.

Wagner, J.R., Brunzelle, J.S., Forest, K.T., and Vierstra, R.D. (2005). A light-sensing knot revealed by the structure of the chromophore-binding domain of phytochrome. Nature *438*, 325-331.

Wagner, J.R., Zhang, J., Brunzelle, J.S., Vierstra, R.D., and Forest, K.T. (2007). High resolution structure of *Deinococcus* bacteriophytochrome yields new insights into phytochrome architecture and evolution. J. Biol. Chem. *282*, 12298-12309.

Wagner, J.R., Zhang, J., von Stetten, D., Gunther, M., Murgida, D.H., Mroginski, M.A., Walker, J.M., Forest, K.T., Hildebrandt, P., and Vierstra, R.D. (2008). Mutational analysis of *Deinococcus radiodurans* bacteriophytochrome reveals key amino acids necessary for the photochromicity and proton exchange cycle of phytochromes. J. Biol. Chem. *283*, 12212-12226.

Yang, X., Kuk, J., and Moffat, K. (2008). Crystal structure of *Pseudomonas aeruginosa* bacteriophytochrome: photoconversion and signal transduction. Proc. Natl. Acad. Sci. USA *105*, 14715-14720.

Yang, X., Kuk, J., and Moffat, K. (2009). Conformational differences between the Pfr and Pr states of *Pseudomonas aeruginosa* bacteriophytochrome. Proc. Natl. Acad. Sci. USA *106*, 15639-15644.

Yang, X.J., Ren, Z., Kuk, J., and Moffat, K. (2011). Temperature-scan cryocrystallography reveals reaction intermediates in bacteriophytochrome. Nature *479*, 428-432.

Figure 1. Burgie *et al.*

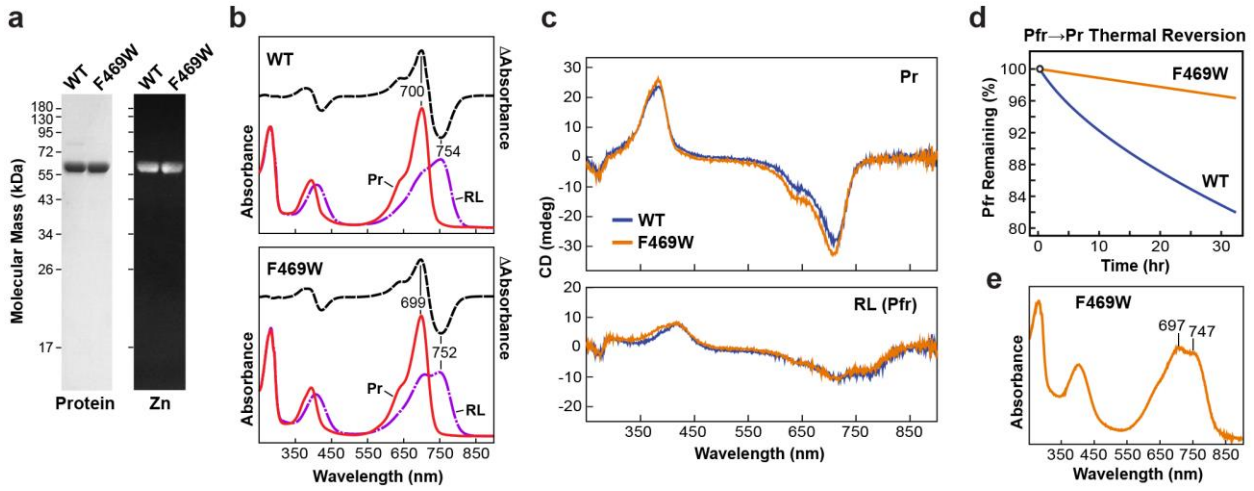

Figure 1. **The PSM of the *Dr*-BphP F469W mutant is photochemically and structurally similar to wild type, but has enhanced Pfr stability**

(A) SDS-PAGE of wild-type (WT) and the F469W PSMs either stained for protein with Coomassie blue (Protein) or for the bound biliverdin by zinc-induced fluorescence (Zn).

(B) UV-visible absorption and difference spectra of the samples in the dark-adapted Pr state or following saturating red-light irradiation (RL, mostly Pfr). Difference spectra (dashed lines at 70% amplitude) were generated by subtracting the RL absorption spectra from those for Pr. Absorption maxima and difference maxima/minima are indicated.

(C) Circular dichroism spectra for the Pr or RL-irradiated samples of WT (blue) or F469W PSMs (orange).

(D) Pfr➔Pr thermal reversion at 25°C of the RL-irradiated WT and F469W PSMs as measured by absorption at 750 nm.

(E) UV-visible absorption spectrum of diffraction quality crystals produced with the F469W(PSM) chromoprotein following saturating RL irradiation (87% Pfr).

Figure 2. Burgie *et al.*

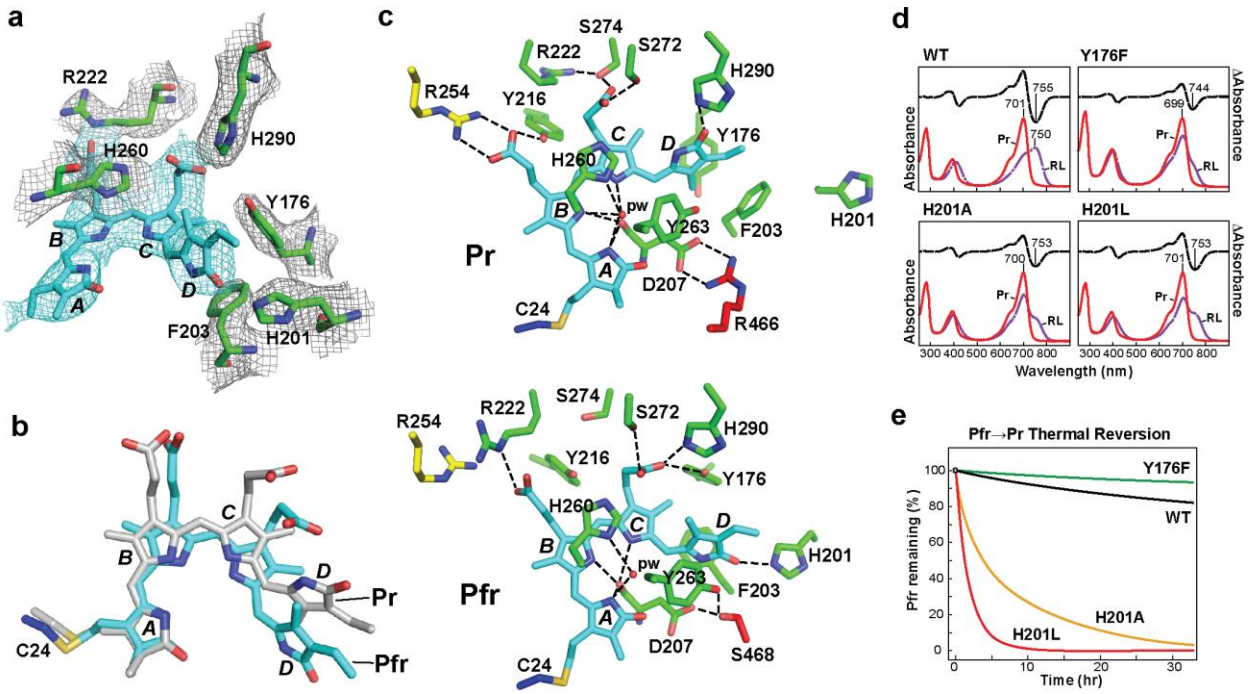

Figure 2. **Photoconversion of *Dr*-BphP from Pr to Pfr includes a *Z*➔*E* D-ring flip and sliding of the bilin within the GAF domain pocket concomitant with rearrangement of surrounding residues**

Carbons are colored by domain/motif: PAS, blue; GAF, green; knot-lasso, yellow; hairpin, red; biliverdin (BV), cyan. Important amino acid contacts and the four pyrrole rings (*A*-*D*) in BV are labeled.

(A and B) Structural arrangement of BV as Pfr within the GAF domain pocket of (A) of Subunit A, or (B) Subunit B. Simulated-annealing omit maps (2Fo-Fc) are shown at 1 σ around BV (magenta) and selected residues (grey).

(C) The relative positions of selected residues surrounding BV in Pr (top) and Pfr (bottom). Dashed lines locate predicted hydrogen bonds. Pyrrole water, pw.

(D) Structural changes/movements in BV induced by Pr➔Pfr photoconversion. Shown are the relative positions of BV in the Pr (grey) and Pfr states (cyan) as revealed following superposition of the GAF domains for Pr (PDB code: 4Q0J (Burgie et al., 2014b)) and Pfr (this work).

(E and F) Y176 and H201 contacting the D pyrrole ring impact *Dr*-BphP photoconversion and Pfr stability. (E) UV-visible absorption spectra of the wild type (WT) and mutant PSMs in the dark-adapted Pr state or following red-light irradiation (RL, mostly Pfr). Absorption maxima/minima are indicated. Difference spectra (dashed lines at 70% amplitude) were

generated by subtracting the RL absorption spectra from those for Pr. (F) Pfr➔Pr thermal reversion at 25°C for the RL-irradiated WT or mutant PSMs as measured by absorption at 750 nm.

See also Figures S1 and S3

Figure 3. Burgie *et al.*

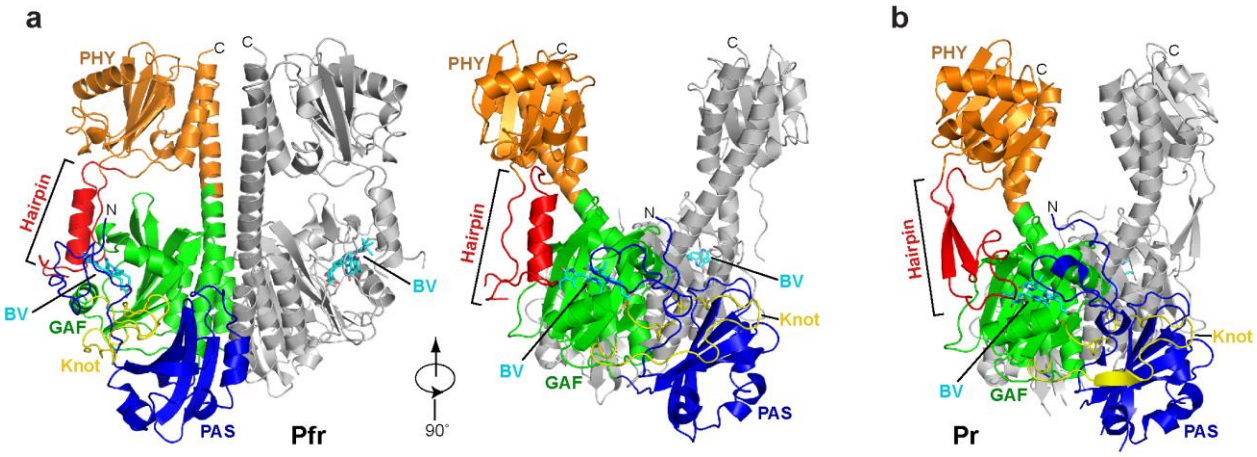

Figure 3 Molecular architecture of the *Dr*-BphP PSM as Pr or Pfr

(A) Two ribbon views of the F469W(PSM) dimer as Pfr. The PAS (blue), GAF (green) and PHY (orange) domains, and the 'knot-lasso' (yellow) and hairpin (red) motifs are colored in the more homogeneous A subunit whereas the sister B subunit is colored in gray. Biliverdin (BV) is colored in cyan. C, carboxy-terminus. N, amino-terminus.

(B) Ribbon view of the PSM from wild-type *Dr*-BphP as Pr (PDB code: 4Q0J (Burgie et al., 2014b)) in the same orientation as the right panel of (A).

See also Figure S2.

Figure 4. Burgie *et al.*

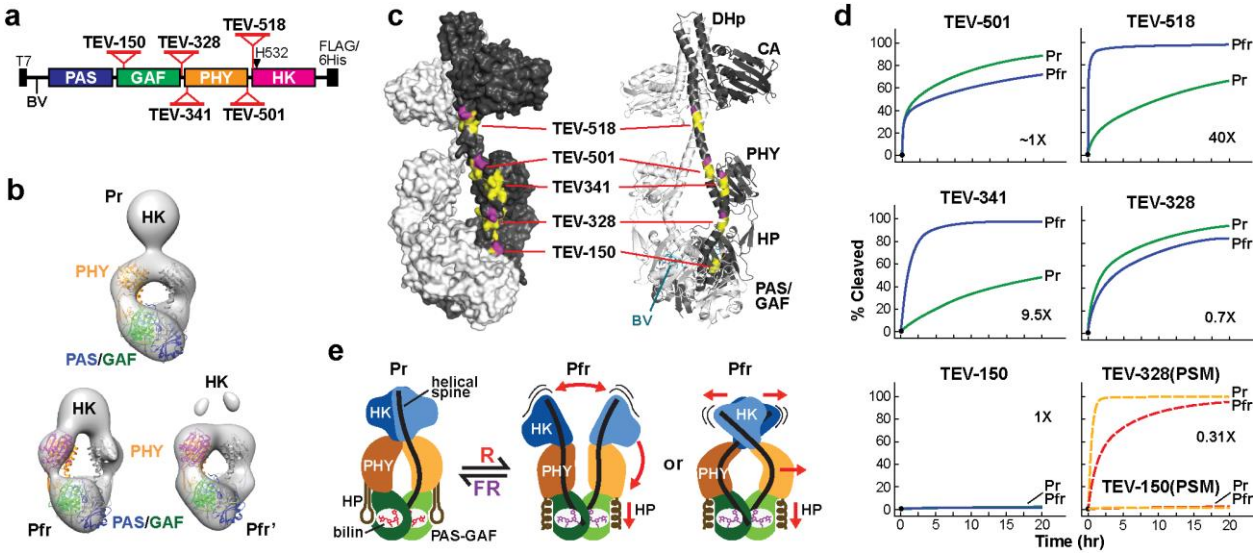

Figure 4 Pfr➔Pr photoconversion perturbs the helical spine of *Dr*-BphP as probed by tobacco etched virus (TEV) protease sensitivity

(A) Domain arrangement of *Dr*-BphP mutants engineered with TEV cleavage sites along the helical spine. The positions of PAS, GAF, PHY and HK domains, the TEV-recognition sites, the terminal T7 and FLAG/6His tags, and the phosphoacceptor hidistine (H532) in the HK domain are indicated.

(B) Single particle EM images of the full-length *Dr*-BphP dimer in the Pr (top) and Pfr or Pfr' states (bottom) as described previously (Burgie et al., 2014b).

(C) Reconstructed surface (left) and ribbon views (right) of the full-length *Dr*-BphP dimer as Pr. The structures were generated by appending the crystal structure of the HK module from *Thermotoga maritima* HK853 (PDB code 3DGE (Casino et al., 2009)) onto the PSM Pr crystal structure (PDB code 4Q0J (Burgie et al., 2014b)), using the Pr EM image shown in (B) as a scaffold (Burgie et al., 2014b). The dimerization/histidine phosphorylation (DHp) and catalytic ATP-binding (CA) domains in the HK module are indicated. The locations of TEV-recognition sites were colored yellow and magenta; the transition from yellow to magenta locates the scissile bond.

(D) Sensitivity of the TEV mutants to TEV protease cleavage as Pr or during continuous red light irradiation (mostly Pfr). Sensitivity of full-length *Dr*-BphP variants as well as the PSMs for

the TEV-150 and TEV-328 constructions (bottom right) are shown. Each time course represents the average of three independent reactions. Relative initial cleavage rates for Pfr as compared to Pr are indicated.

(E) Possible cooperative 'toggle' models for the conformational changes induced by Pr➔Pfr photoconverion of *Dr*-BphP. The dimeric architecture of Pr rearranges upon photoconversion via β-strand to α-helical contraction of the hairpin stem concomitant with helical spine splaying to either completely separate the sister OPMs or to force their repositioning through a scissor-like pivot near residue 501 in the helical spine. The end result is to alter the relative position of the sister HK domains to either discourage or promote a light-regulated HK phosphorelay. See also Figure S4.

Table 1. X-ray Diffraction Data Collection and Refinement Statistics for the PSM Structure of *Dr*-BphP(F469W) as Pfr.

Data collection[a]	
Space group	$P2_12_12_1$
Cell dimensions	
a, b, c (Å)	89.4, 192.7, 225.1
α, β, γ (°)	90, 90, 90
Resolution (Å)	58.8-3.31 (3.43-3.31)
R_{merge}	0.120 (1.50)
$CC_{1/2}$	0.998 (0.440)
$I/\sigma(I)$	11.9 (1.7)
Completeness (%)	88 (23)
Redundancy	8.1 (7.1)
Wilson B-factor	123.7
Refinement	
Resolution (Å)	48.8-3.31 (3.43-3.31)
No. reflections	51,712 (1,381)
R_{work} / R_{free}	0.196 / 0.232[b]
No. atoms	
Protein	14,739
Ligand[c]	192
Water	20
B factors	
Overall	153.8
Protein	154.0
Ligand	140.8
Water	128.4
Geometry	
R.M.S deviations	
Bond lengths (Å)	0.002
Bond angles (°)	0.58
Ramachandran	

Favored (%) Outliers (%)	98.5 0.0
Clash score	7.0

[a]Outer shell values are in parentheses.

[b]Test set for R_{free} calculation was chosen randomly and comprised 3.6% of the total number of reflections

[c]This includes atoms from 4 BV, 2 acetate, 2 ethylene glycol, and 5 glucose molecules.